Millimeter-Wave Resonant Beam SWIPT

Shuaifan Xia, Qingwei Jiang, Wen Fang, Qingwen Liu, *Senior Member IEEE*, Shengli Zhou, *Fellow IEEE*, Mingqing Liu, and Mingliang Xiong

***Abstract*—The rapid expansion of the Internet of Things (IoT) necessitates robust solutions for charging and communicating with a multitude of devices, making simultaneous wireless information and power transfer (SWIPT) technology increasingly vital. However, existing methods can hardly provide high charging power, great channel capacity, and flexible mobility at the same time. This manuscript introduces a millimeter wave resonant beam system for SWIPT (mmRB-SWIPT), leveraging retro-directive antenna arrays to enable automatic beam alignment and enhanced transmission efficiency without additional controls. A dual-frequency design allows the system to operate in a frequency division duplex mode, thereby resolving the echo interference issues encountered in prior resonant beam systems. Analytical models are developed to evaluate the system's viability and performance, with numerical analysis indicating the capability to transmit watt-level power and achieve 4.8bps/Hz of spectral efficiency in indoor settings.**

***Index Terms*—Resonant beam system, retro-directive antenna, Simultaneous wireless information and power transfer, Millimeter wave.**

I. Introduction

THE Internet of Things (IoT) has been seen as one of the key innovative application scenarios for the next-generation network [1]. IoT devices, which are typically embedded in various environments ranging from domestic to industrial settings, rely on constant power and communication capabilities to perform their functions effectively. The ability to wirelessly charge these devices while simultaneously transmitting data is crucial for ensuring seamless operation in areas where conventional cables and batteries are cumbersome or impossible [2], [3].

Simultaneous wireless information and power transfer (SWIPT) emerge as an enabling technology in IoT scenarios where constant charging and communication services are desired [4]. Radio frequency (RF) based SWIPT is especially advantageous since RF energy is more controllable [5], and has fewer limitations on device mobility [2]. However, a significant drawback of RF-based far-field SWIPT systems is the relatively low transmission efficiency and the limited charging power they offer (typically several milliwatts [3]), which may not be sufficient for sustaining long-term device operation without supplementary power sources. The over-the-air transmission efficiency is seen as the bottleneck for RF-based wireless power transmission [6].

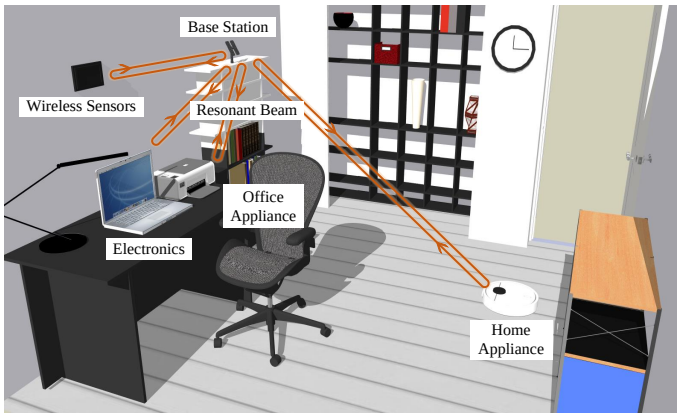

Fig. 1. A typical application scenario of the proposed system.

Featuring higher transmission power and focused laser beam, laser-based SWIPT technologies have introduced promising alternatives. Yet complex beam tracking and control mechanisms prevent the wide adoption of laser-based SWIPT. The optical resonant beam system (RBS) was proposed as an effective alternative to traditional SWIPT [7]–[9]. By employing retro-reflectors on both the transmitter and the receiver, the lightwave can automatically follow the device's movement, realizing self-alignment. A similar structure operating at RF frequency has also been explored to provide wireless power transfer with higher efficiency [10]. The retro-reflective approach allows the system to refine the power circulating between the transmitter and the receiver, finally reaching an optimal state with a power-focused beam. However, the retro-directive beam subject the system to severe echo interference, i.e., the inbound and outbound beams interfere with each other, hindering the communication [11], [12].

Millimeter wave (mmWave), recently regarded as one of the promising candidates for 6G mobile networks [13], is characterized by narrow beam transmission [14]. Despite a troublesome beam alignment [15], mmWave is potent for achieving higher power transmission efficiency and higher data rate [16]. With the resonance mechanism from the optical RBS, the beam alignment issue of mmWave can be tackled similarly.

In this manuscript, we propose the millimeter wave resonant beam SWIPT system (mmRB-SWIPT) featuring higher power efficiency and obviating the need for beam alignment. Phase

Shuaifan Xia, Qingwei Jiang, and Qingwen Liu are with the College of Electronic and Information Engineering, Tongji University, Shanghai 201804, China (e-mail: {collinxia, jiangqw, qliu}@tongji.edu.cn).

Wen Fang is with the School of Electronic Information and Electrical Engineering, Shanghai Jiao Tong University, Shanghai 200240, China (email:wendyfang@sjtu.edu.cn).

Shengli Zhou is with the Department of Electrical and Computer Engineering, University of Connecticut, Storrs, CT 06269, USA (email:shengli.zhou@uconn.edu).

Mingqing Liu is with Li-Fi Research and Development Centre, University of Cambridge, Cambridge, UK (email: ml2176@cam.ac.uk).

Mingliang Xiong is with Hangzhou Institute of Extremely-Weak Magnetic Field Major National Science and Technology Infrastructure, Hangzhou 310052, China (email:xiongml@foxmail.com).

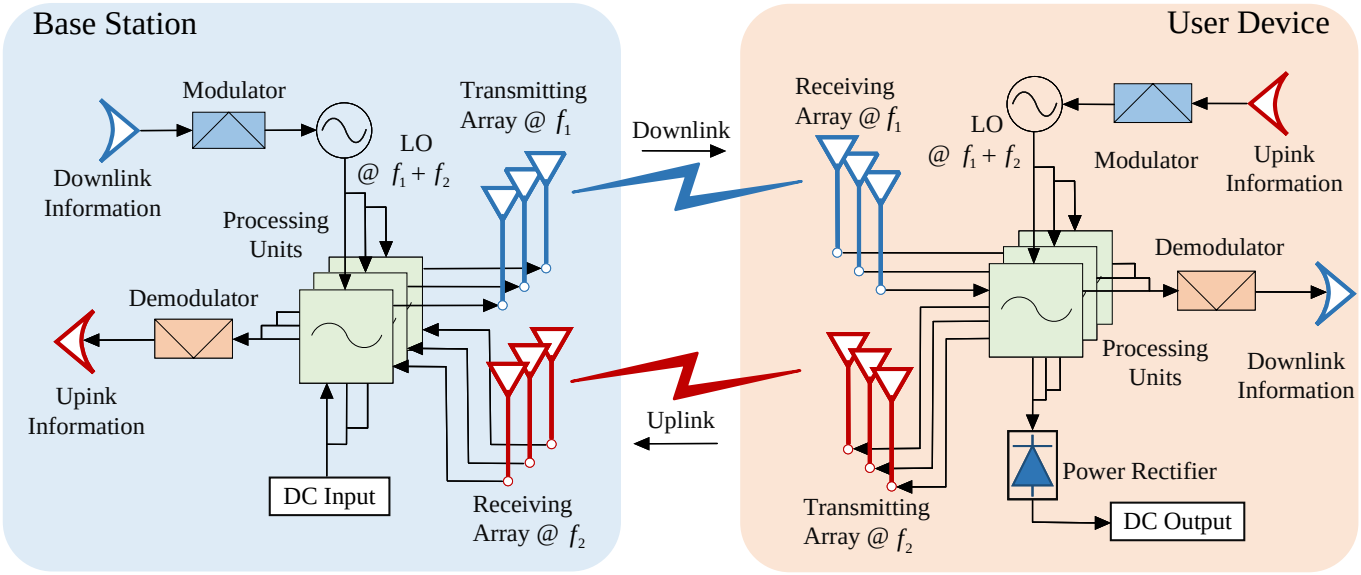

Fig. 2. Schematic of the system.

conjugation-based retro-directive antenna arrays are adopted to make the incoming signal retrace its way. Resembling the structure of optical RBS, we equip both the base station (BS) and the user device (UD) with retro-directive ability, enabling the beam to align automatically and follow the device inherently. A special design to separate the frequencies for downlink and uplink is introduced to address the challenge of echo interference faced by the optical RBS.

Analytical models are established by incorporating conventional electromagnetism theories and the principles from optical RBS. The function details of mmRB-SWIPT are closely examined to demonstrate the feasibility and novelty. Numerical simulations suggested that the mmRB-SWIPT can deliver approximately 1W of charging power and enables 4.8bps/Hz of channel spectral efficiency with less than 1μs to setup.

The contributions of this manuscript are as follows:

c1) The proposed mmRB-SWIPT can deliver higher charging power with greater transmission efficiency without the extra need for beam control mechanisms.
c2) A dual-frequency design is introduced to realize duplex communication, eliminating the echo interference faced by RBS.
c3) We propose analytical models to explicate the resonance mechanism, with which the system's status and performance can be numerically determined.

The rest of the paper is organized as follows. We first illustrate the design architecture and working principle of the proposed mmRB-SWIPT in Section II. Then, analytical models are established in Section III. to investigate the resonant behavior and communication channel of the system. In Section IV, we demonstrate the initialization process, power transmission efficiency, and communication performance through a series of simulations. Other aspects of interest are discussed in Section V. Finally, we conclude the manuscript in Section VI with prospective future works.

II. System Design

In this section, the resonance mechanism is explored to illustrate the self-converging feature of the proposed system providing the foundation for further investigation. Phase conjugation-based retro-directive antenna array is studied to show the operating principle of the system. To eliminate the echo interference introduced by the resonance, a dual-frequency scheme is proposed to provide interference-free frequency division duplexing communication.

A. Resonant Beam System

As shown in Fig. 2, the system consists of a base station and one or more user-end device(s). Each device comprises both a transmitting (Tx) antenna array and a receiving (Rx) antenna array operating at different but corresponding frequencies. The arrays are designed to re-transmit the incoming signal back along its original path, of which the principle is detailed in the next subsection.

The BS is equipped with a direct current (DC) input source for energy supply and information modulation/demodulation components for communication purposes. Processing units are connected to antenna units, in charge of power dividing and signal mixing. The signal received by the BS is divided into two parts: a small portion is used to demodulate uplink information sent by the UD, and the rest of the signal is to be phase conjugated, modulated, and transmitted to the UD. The UD shares a similar structure with a power rectifier for harvesting the energy as DC output. The signal arriving at UD is divided into three parts, where a large portion is sent to the power rectifier for the charging power output, with the rest of the signal being processed similarly to the BS, i.e., one part for demodulation, one part for phase conjugation, modulation, and re-transmission.

Initially, the UD radiates an omnidirectional pilot signal. The Rx array on the BS side receives a part of the broadcasting

signal, with each antenna unit acquiring a unique phase, indicating the direction of the beam. Phase conjugation and power amplification are subsequently applied to the signal, before which the Tx array of BS transmits a signal with higher power and exactly opposite direction as the pilot signal.

The above procedure has been extensively applied in retro-directivity-based wireless power transfer techniques, where the UD continues to radiate the omnidirectional signal intermittently [17]–[19]. Being different from these schemes, the UD of our proposed system is equipped with a similar set of components as the BS and performs phase conjugation for the receiving signals as well. The process of the signal starting from the Tx array of UD, reaching BS, being phase conjugated and retro-directed, and finally returning to the UD is defined as an iteration. With several iterations, the phases on the antenna arrays align with each other, making the power beams eventually converge and no longer change in future iterations. This convergence, shown in Fig. 3, forms a power-concentrated strip between the BS and UD, known as the *resonance*.

The resonance is the key feature that distinguishes RBS from conventional beamforming systems. It allows the radiated power to be focused on the shortest path between BS and UD. Moreover, due to the continual reflection of the signal within the power strip, the system benefits from a self-aligning capability, enabling unrestricted movement of the UD within a defined Field-of-View (FoV) without necessitating additional tracking or beam steering mechanisms.

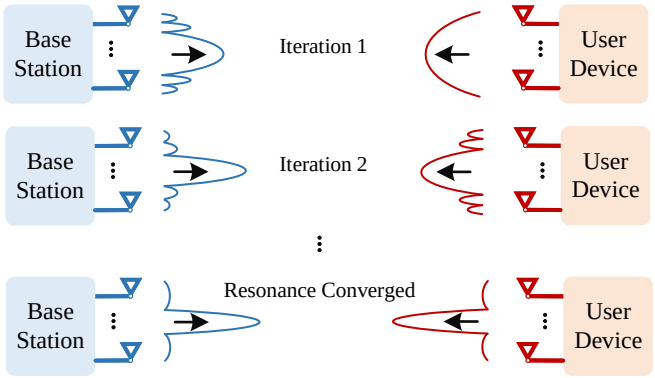

Fig. 3. Beam pattern converges across successive iterations.

B. Phase Conjugation Enabled Retro-Directivity

1) Principle of Phase Conjugation: Retro-directive antenna (RDA) arrays are employed to empower the BS and UD to transmit the received signal retracing its back back, forming the resonance. Phase conjugation and Van-atta array are two dominant approaches to the retro-directivity [20]. With a heterodyning method, the phase conjugation can provide both retro-directivity and information modulation [21], [22], which are desirable in our system.

The basic concept of phase conjugation is to invert the phase of the received signal and re-transmit. For an electromagnetic (EM) wave with the form

$$\mathbf{E} = A(\mathbf{r})e^{j(k\mathbf{r}+\omega t)}, \tag{1}$$

where $A(\mathbf{r})$ amplitude of the field at the specific point indicated by the position vector $\mathbf{r}$, k is the wave number, and ω is the angular frequency. The phase conjugate of $\mathbf{E}$ can be represented as [23]:

$$\mathbf{E}^* = A(\mathbf{r})e^{-j(k\mathbf{r}+\omega t)}. \tag{2}$$

The obtained EM wave is with the same amplitude and inverted phase. In a reciprocal environment, the phase-conjugated wave will retrace its way back to its source while retaining the same frequency and amplitude.

The heterodyne approach for phase conjugation is adopted in the proposed system, where the received signal is mixed with a local oscillator (LO) [22].

2) Retro-directive Array with Different Frequencies: Despite the power-concentration and self-aligning features of the resonance, it is accompanied by a significant drawback, the echo interference problem. The repeated reflection of signals along the resonant path leads to inevitable collisions between the downlink (BS to UD) and uplink (UD to BS) signals. When signals share the same frequency, interference ensues. To mitigate this challenge, our proposed system incorporates a frequency division scheme, separating the downlink and uplink frequencies. Additionally, a dual-frequency design is employed to preserve retro-directivity while addressing the interference concern.

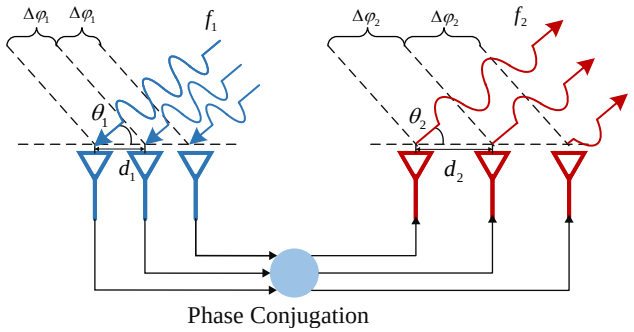

Fig. 4. Maintaining retro-directivity with different frequencies.

Since our system is designed to provide far-field SWIPT in the indoor environment, the transmission distance L between BS and UD is supposed to satisfy the far-field region requirement, that is

$$L > \frac{2D^2}{\lambda}, \tag{3}$$

where D denotes the maximum dimension of the antenna, and λ denotes the operating wavelength.

Under such conditions, the incoming waves can be approximated to plane waves. Consider the case of a uniform linear array (ULA), as demonstrated in Fig. 4, the signal at frequency f_1 arrives at the array, having an incident angle θ_1. Since the interval between adjacent antenna units is constant d_1, the intercepted phases of adjacent units are of constant value as well, denoted as $\Delta\varphi_1$, and can be calculated as

$$\Delta\varphi_1 = \frac{2\pi d_1}{\lambda_1}\cos\theta_1, \tag{4}$$

where λ_1 denotes the wavelength of the incoming signal.

With the basic principle of phase conjugation, we can obtain a signal propagating along the opposite direction by having the transmitting antenna units have a phase difference $\Delta\varphi_2$ exactly the opposite of $\Delta\varphi_1$. Re-transmitted signals from antenna units can interfere with each other and form the beam pattern retracing its way. However, as mentioned before, to avoid subjecting the communication to echo interference, the downlink and uplink should have different operating frequencies. With modified frequency, the interference-based retro-directivity is compromised, culminating in deviation from the desired path.

To maintain the retro-directivity with altered frequency f_2, the goal is to make the transmitting angle θ_2 equal to the incident angle θ_1. We have:

$$\begin{cases} \theta_1 = \arccos\left(\dfrac{\Delta\varphi_1}{2\pi}\dfrac{\lambda_1}{d_1}\right) \\ \theta_2 = \arccos\left(\dfrac{\Delta\varphi_2}{2\pi}\dfrac{\lambda_2}{d_2}\right) \end{cases}. \tag{5}$$

Hence, by ensuring that the spacing between adjacent antenna units is proportional to the respective frequencies, i.e., $\lambda_1/d_1 = \lambda_2/d_2$, we will have $\theta_1 = \theta_2$, thus maintaining the retro-directivity with different Tx and Rx frequencies [24].

This spacing arrangement remains applicable to uniform rectangular array (URA) employed in the proposed system. Consider a URA whose the spacing in the x-direction is d_{x1} and in the y-direction is d_{y1}. The phase difference between adjacent elements in the x-direction and the y-direction can be calculated as

$$\begin{cases} \Delta\varphi_{x1} = \dfrac{2\pi d_{x1}}{\lambda_1}\sin\theta_1\cos\phi_1 \\ \Delta\varphi_{y1} = \dfrac{2\pi d_{y1}}{\lambda_1}\sin\theta_1\sin\phi_1 \end{cases}, \tag{6}$$

where θ_1 and ϕ_1 are the elevation and azimuth angle of the incoming wave at frequency f_1.

For the outgoing wave to have the same azimuth angle $\phi_2 = \phi_1$ and elevation angle $\theta_2 = \theta_1$ at frequency f_2, we require:

$$\begin{cases} \Delta\varphi_{x2} = \dfrac{2\pi d_{x2}}{\lambda_2}\sin\theta_2\cos\phi_2 \\ \qquad = -\dfrac{2\pi d_{x1}}{\lambda_1}\sin\theta_1\cos\phi_1 = -\Delta\varphi_{x1} \\ \Delta\varphi_{y2} = \dfrac{2\pi d_{y2}}{\lambda_2}\sin\theta_2\sin\phi_2 \\ \qquad = -\dfrac{2\pi d_{y1}}{\lambda_1}\sin\theta_1\sin\phi_1 = -\Delta\varphi_{y1} \end{cases}. \tag{7}$$

Since we have $\lambda_1 \neq \lambda_2$, the spacing for the URA at frequency f_2 must satisfy

$$\frac{\lambda_1}{\lambda_2} = \frac{d_{x1}}{d_{x2}} = \frac{d_{y1}}{d_{y2}}, \tag{8}$$

where d_{x2} is the spacing for the x-direction and d_{y2} is for the y-direction.

This dual-frequency scheme not only addresses the challenge of echo interference faced by the optical RBS, but also provides isolation between Tx and Rx signal chains during simultaneous transmission and reception [25], achieving frequency division full-duplex transmission.

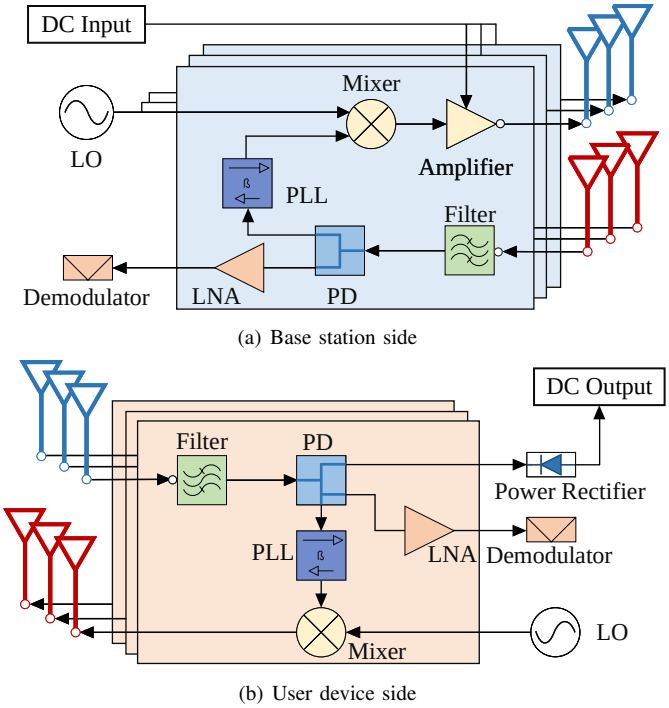

(a) Base station side

(b) User device side

Fig. 5. Detailed illustration of the processing units.

C. Information Transmission and Carrier Synchronization

1) Carrier Synchronization and Modulation: In our system, as indicated in Fig. 2, the Tx array of BS and Rx array of UD (the downlink array pair) are configured to operate at f_1, and the Rx array of BS and Tx array of UD are configured to operate at f_2. After the resonance converges, the communication initiates.

To provide a synchronized phase for retro-directivity and pure carrier wave for information bearing, phase-locked loops (PLL) are employed. The processing units connected to every antenna element comprise a filter, a PLL, a low noise amplifier (LNA), and a mixer, as illustrated in Fig. 5. The locked carrier wave is also used to perform coherent demodulation to retrieve the inbound information.

The BS receives the uplink signal at f_2, of which the majority is directed to the PLL for synchronization. The rest of it, split by the power divider (PD), is amplified by an LNA and utilized for information demodulation. After carrier synchronization, the resulting signal from PLL is mixed with LO at $f_1 + f_2$ for heterodyning. Additionally, the LO signal is pre-modulated with the downlink information. Following proper mixing and filtering, the signal is shifted to frequency f_1, with its phase conjugated, and carries the downlink information. Finally, the DC input is applied to amplifiers within the processing units to provide power.

Consider the m-th element on the BS side, the received uplink signal is in the form

$$\begin{aligned} u(t) =& x^{\mathrm{u}}(t)\cos(2\pi f_2 t + \varphi_m) \\ &+ y^{\mathrm{u}}(t)\sin(2\pi f_2 t + \varphi_m) \end{aligned}, \tag{9}$$

with $x^{\mathrm{u}}(t)$ and $y^{\mathrm{u}}(t)$ representing the in-phase and quadrature components of the uplink modulated signal, respectively. For

downlink information bearing, PLL recovers a pure carrier wave at frequency f_2

$$c(t) = \cos(2\pi f_2 t + \varphi_m), \tag{10}$$

where φ_m is the phase term of this element. The LO signal to be mixed with is already modulated with downlink information and is in the form

$$\begin{aligned} L(t) =& x^{\mathrm{d}}(t)\cos(2\pi(f_1+f_2)t) \\ &+ y^{\mathrm{d}}(t)\sin(2\pi(f_1+f_2)t) \end{aligned}, \tag{11}$$

where $x^{\mathrm{d}}(t)$ and $y^{\mathrm{d}}(t)$ are the in-phase and quadrature components of the signal to be sent downlink, respectively. With heterodyne, the resultant signal is

$$\begin{aligned} r(t) =& \frac{1}{2}x^{\mathrm{d}}(t)\left[\cos(2\pi f_1 t - \varphi_m) + \cos(2\pi(f_1+2f_2)t + \varphi_m)\right] \\ &+ \frac{1}{2}y^{\mathrm{d}}(t)\left[\sin(2\pi f_1 t - \varphi_m) + \sin(2\pi(f_1+2f_2)t + \varphi_m)\right] \end{aligned}. \tag{12}$$

The signal centered at frequency $f_1 + 2f_2$ can be easily removed with bandpass filter. The final signal entering the m-th antenna element is

$$\begin{aligned} d(t) =& x^{\mathrm{d}}(t)\cos(2\pi f_1 t - \varphi_m) \\ &+ y^{\mathrm{d}}(t)\sin(2\pi f_1 t - \varphi_m) \end{aligned}. \tag{13}$$

Comparing (9) with (13), we can see that $d(t)$ is phase-conjugated version of $u(t)$ and modulated with downlink information.

On the UD side, the arriving signal at f_1 is divided into three parts after filtering: the majority is harvested for charging power output, a small portion is used for demodulating the received information, and an extremely small fraction is routed to the PLL for phase recovery. The similar approach to phase conjugation and modulation also applies on the UD side, the output of PLL is then mixed with modulated LO at $f_1 + f_2$ to provide a phase-conjugated and information-bearing signal.

2) Multiple Access: The resonance mechanism allows the BS to establish resonance with multiple UDs simultaneously [26], [27], making it possible to provide SWIPT service to multiple users with only one BS. However, due to the possibly unknown UD-BS relative location, the signal from each UD needs to be processed individually and exclusively to realize the retro-directivity thus maintaining the stable resonance. To this end, time division multiple access (TDMA) can be adopted. Upon receiving pilot signals from more than one UDs, the BS can formulate frame-based scheduling scheme to allow multiple access.

Consider the transmission from BS as a series of frames. Each frame is composed of $n+1$ time slots given the number of users n. During the time slot designated to the i-th user, the BS will only process the signal from it and disregard all other signals. Also, after being assigned to specific time slot, the UD should be idle during others' time slot to avoid possible interference. In the last time slot of each time frame, the BS is configured to listen for request to initialize link from other possible users. Despite the complexity, this TDMA implementation not only allows the BS to provide service to multiple users simultaneously, but also reduces the possible interference.

The power allocation is primarily based on the scheduling algorithm adopted by BS, which may vary depending on the specific need of the application scenario. For example, in a smart home scenario, computers may have access to more time slots and/or with longer duration while time slots for home accessories may be shorter. More sophisticated scheduling techniques can be explored to better conform to the specific application scenario.

III. Analytical Models

In this section, analytical models are established to provide insight into the system's performance. Starting from the power transmission, the resonance initialization is explicated, with an examination of the impact of possible phase offsets and noises.

A. Power Transmission and Harvesting

Transmission and harvesting of power begins at the first iteration. Energy-bearing beam arriving at UD is always harvested with a fixed ratio, with only α of the total received power sent back. This subsection examines the power transmission and propagation process for a single-bound trip, the analytical model built is applicable for both downlink and uplink.

Without losing generality, suppose the numbers of antenna units in the Tx array and Rx array are M and N, respectively. In the context of linearly polarized plane electromagnetic waves, the Poynting vector $\mathbf{S}$, with its magnitude representing the power density W, is given as [28] eq. (9.10):

$$|\mathbf{S}| = W = \frac{1}{2\mu c}\mathbf{E}^2, \tag{14}$$

where $\mathbf{E}$ is the complex amplitude of the electric field, μ is the permeability of vacuum, and c is the speed of light. The electric field radiated by the m-th Tx unit and received by the n-th Rx unit can be given as [29]:

$$\mathbf{E}_{mn} = \sqrt{2\mu c W_{mn}}\, e^{-j(k\mathbf{r}_{mn} - \varphi_m)}, \tag{15}$$

with $\mathbf{r}_{mn}$ representing a vector starting from the m-th Tx unit to the n-th Rx unit, and φ_m denoting the initial phase. W_{mn} is the received power from the m-th Tx unit to the n-th Rx unit.

In our case, since only the far-field region is of interest, the Friis' equation can be employed to derive W_{mn} as [30] eq. (7.14):

$$W_{mn} = \frac{P_{\mathrm{T}_m} G_{\mathrm{T}_m}(\theta_{mn}, \phi_{mn})\, G_{\mathrm{R}_n}(\theta_{mn}, \phi_{mn})\, \lambda^2}{4\pi|\mathbf{r}_{mn}|^2 \times \left(4\pi|\mathbf{r}_{mn}|\right)^2}, \tag{16}$$

with P_{T_m} denoting the emitted power from the m-the Tx unit, λ denoting the operating wavelength, $G_{\mathrm{T}_m}(\theta_{mn}, \phi_{mn})$ representing the Tx gain of the m-th Tx unit in the direction of the n-th Rx unit, and $G_{\mathrm{R}_n}(\theta_{mn}, \phi_{mn})$ having the similar definition. The gains are determined by the relative location between the m-th Tx unit and the n-th Rx unit as functions of azimuth angle θ_{mn} and elevation angle θ_{mn}. For simplicity, the gains will be denoted as $G_{\mathrm{T}_{mn}}$ and $G_{\mathrm{R}_{mn}}$ without causing ambiguity. The Tx units of BS and UD are considered identical with the gain G_{T}, the same assumption applies to the Rx units.

With (15) and (16), the electric field $\mathbf{E}_{mn}$ can be explicitly derived as:

$$\mathbf{E}_{mn} = \sqrt{2\mu c \frac{P_{\mathrm{T}_m} G_{\mathrm{T}_{mn}} G_{\mathrm{R}_{mn}}}{4\pi |\mathbf{r}_{mn}|^2}} \frac{\lambda}{4\pi |\mathbf{r}_{mn}|} e^{-j(k\mathbf{r}_{mn} - \varphi_m)}. \quad (17)$$

Considering there are M Tx units, the total power received by the n-th Rx antenna can be calculated by summing the contributions from all M units. That is:

$$\begin{aligned} P_{\mathrm{R}_n} &= \frac{4\pi}{2\mu c} \left| \sum_{m=1}^{M} |\mathbf{r}_{mn}| \mathbf{E}_{mn} \right|^2 \\ &= \frac{\lambda^2}{16\pi^2} \left| \sum_{m=1}^{M} \frac{\sqrt{P_{\mathrm{T}_m} G_{\mathrm{T}_{mn}} G_{\mathrm{R}_{mn}}}}{|\mathbf{r}_{mn}|} e^{-j(k\mathbf{r}_{mn} - \varphi_m)} \right|^2, \end{aligned} \quad (18)$$

where each m-th Tx antenna element is considered individually.

Finally, the power received by the Rx array with a total of N antenna elements can be calculated by summing the power received by each Rx antenna element as

$$\begin{aligned} P_{\mathrm{R}} &= \sum_{n=1}^{N} P_{\mathrm{R}_n} \\ &= \frac{\lambda^2}{16\pi^2} \sum_{n=1}^{N} \left| \sum_{m=1}^{M} \frac{\sqrt{P_{\mathrm{T}_m} G_{\mathrm{T}_{mn}} G_{\mathrm{R}_{mn}}}}{|\mathbf{r}_{mn}|} e^{-j(k\mathbf{r}_{mn} - \varphi_m)} \right|^2. \end{aligned} \quad (19)$$

In the above derivation, the total received power by the antenna array is calculated by taking summation on each antenna element. Since the power relationship is based on the gain of the single antenna element, the far-field requirement applies to the size of the single antenna element, not the antenna array [29]. Suppose the transmission distance is L, the largest dimension of a single antenna element is D_{ele}, and the one of the antenna array is D_{arr}. In instances where $D_{\mathrm{ele}}^2/\lambda \ll L \ll D_{\mathrm{arr}}^2/\lambda$, the approach remains applicable.

With this representation of the total received power, the transmission efficiency η can be obtained:

$$\eta = \frac{\lambda^2 \sum_{n=1}^{N} \left| \sum_{m=1}^{M} \frac{\sqrt{P_{\mathrm{T}_m} G_{\mathrm{T}_{mn}} G_{\mathrm{R}_{mn}}}}{|\mathbf{r}_{mn}|} e^{-j(k\mathbf{r}_{mn} - \varphi_m)} \right|^2}{16\pi^2 \sum_{m=1}^{M} P_{\mathrm{T}_m}}. \quad (20)$$

And we can have the path loss $\delta = 1 - \eta$. Notably, the transmission efficiency calculated in (20) only accounts for a single trip from the designated Tx side to the respective Rx side. In the systematic analysis, both the path losses for downlink and uplink should be examined individually.

B. Resonance Establishment

1) Self-reproducing Resonance: With both BS and UD equipped with retro-directive antenna arrays, the power flows bidirectionally. During each iteration, the phases of antenna elements undergo refinement, reducing the disparity between the received electric field across two consecutive iterations, ultimately converging to a negligible value. Subsequently, the distribution stabilizes and is repeatedly produced in further iterations. The stabilized power distribution is described as *self-reproducing*.

The establishment of a stable resonance requires that the transmission distance to be integer multiples of wavelength. In the initialization process, the signal with a certain bandwidth is transmitted. The actual frequency of the signal would drift around its central frequency to adapt the transmission distance, and finally reach a stability to meet the wavelength criterion in accordance with the actual transmission distance.

The number of Tx and Rx units within the same device are matched. Suppose there are N Tx units and Rx units on UD, and M for BS. Let us denote the complex amplitude of the signal from the n-th Tx units of UD in the i-th iteration as $\mathbf{E}_{i,n}^{\mathrm{UD}}$. The signal received by the m-th Rx units of BS, undergoing phase conjugation, and transmitted by the m-th Tx units of BS can be represented as:

$$\mathbf{E}_{i,m}^{\mathrm{BS}} = G_{\mathrm{T}_m} \mathcal{P} \left\{ \left[\sum_{n}^{N} G_{\mathrm{R}_{nm}} \mathbf{E}_{i,n}^{\mathrm{UD}} \right]^* \right\}. \quad (21)$$

where $*$ denotes the phase conjugation operation, $\mathcal{P}\{\cdot\}$ denotes the aggregate power amplification function. The superimposed wave emitting from BS can be calculated and simplified as:

$$\begin{aligned} \mathbf{E}_{i}^{\mathrm{BS}} &= \sum_{m}^{M} G_{\mathrm{T}_m} \mathcal{P} \left\{ \left[\sum_{n}^{N} G_{\mathrm{R}_{nm}} \mathbf{E}_{i,n}^{\mathrm{UD}} \right]^* \right\}, \\ &= G_{\mathrm{T}} \mathcal{P} \left\{ \left[G_{\mathrm{R}} \mathbf{E}_{i}^{\mathrm{UD}} \right]^* \right\} \end{aligned} \quad (22)$$

where $\mathbf{E}_{i}^{\mathrm{UD}} = \sum_{n}^{N} G_{\mathrm{R}_{nm}} \mathbf{E}_{i,n}^{\mathrm{UD}}$ is the vector summation of the fields emitted from every unit on UD.

Similarly, the signal from the n-th Tx units of UD in the $i+1$-th iteration can be represented recursively as

$$\begin{aligned} \mathbf{E}_{i+1,n}^{\mathrm{UD}} &= G_{\mathrm{T}_n} \mathcal{H} \left\{ \left[\sum_{n}^{N} G_{\mathrm{R}_{mn}} \mathbf{E}_{i,m}^{\mathrm{BS}} \right]^* \right\} \\ &= G_{\mathrm{T}_n} \mathcal{H} \left\{ \left[\sum_{m}^{M} G_{mn}^{\mathrm{down}} \mathcal{P} \left\{ \left[\sum_{n}^{N} G_{\mathrm{R}_{nm}} \mathbf{E}_{i,n}^{\mathrm{UD}} \right]^* \right\} \right]^* \right\}, \end{aligned} \quad (23)$$

where $\mathcal{H}\{\cdot\}$ is the aggregate power harvesting function, and $G_{mn}^{\mathrm{down}} = G_{\mathrm{R}_{mn}} G_{\mathrm{T}_{mn}}$. From the array perspective, the electric wave ultimately emitted from the UD in the $i+1$-th iteration can be obtained:

$$\begin{aligned} \mathbf{E}_{i+1}^{\mathrm{UD}} &= \sum_{n}^{N} \mathbf{E}_{i+1,n}^{\mathrm{UD}} = G_{\mathrm{T}} \mathcal{H} \left\{ \left[G_{\mathrm{R}} \mathbf{E}_{i}^{\mathrm{BS}} \right]^* \right\} \\ &= G_{\mathrm{T}} \mathcal{H} \left\{ \left[G_{\mathrm{R}} G_{\mathrm{T}} \mathcal{P} \left\{ G_{\mathrm{R}} \mathbf{E}_{i}^{\mathrm{UD}^*} \right\} \right]^* \right\} \end{aligned}. \quad (24)$$

Suppose the system converges on the iteration k, according to the resonance principle, the field distribution on the iteration $k+1$ should remain the same, i.e.

$$\mathbf{E}_{k+1}^{\mathrm{UD}} = G_{\mathrm{T}} \mathcal{H} \left\{ \left[G_{\mathrm{R}} G_{\mathrm{T}} \mathcal{P} \left\{ G_{\mathrm{R}} \mathbf{E}_{k}^{\mathrm{UD}^*} \right\} \right]^* \right\} = \mathbf{E}_{k}^{\mathrm{UD}}. \quad (25)$$

Upon obtaining (25), it can be determined that a stable resonance is reached, and the electric fields are to reproduce themselves in further iterations.

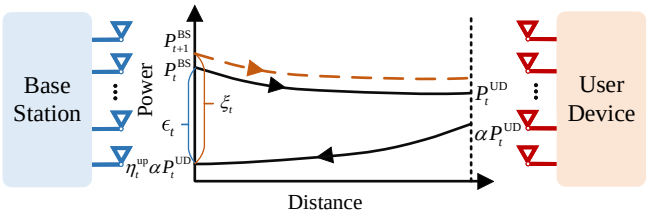

Fig. 6. Power circulation within the system.

Another simpler but still effective perspective to examine the self-reproducing resonance is through the power circulation, as illustrated in Fig. 6. Suppose the DC input on the BS side supplies the system with adequate power allowing the power amplifiers to function. On the iteration t, BS transmits signal with total power of P_i^{BS}, the power received on the UD side is

$$P_t^{\mathrm{UD}} = \eta_t^{\mathrm{down}} P_t^{\mathrm{BS}}, \tag{26}$$

where η_t^{down} is the downlink transfer efficiency calculated with (20).

UD harvests the majority of the received power and returns a small portion with a power return ratio α. Thus, in $t+1$-th iteration, the power emitted from BS is

$$P_{t+1}^{\mathrm{BS}} = g(\eta_t^{\mathrm{up}} \alpha P_t^{\mathrm{UD}}), \tag{27}$$

where $g(\cdot)$ is the power gain function determined by the power amplifier. In a specific iteration t, we denote the difference between the power emitted from BS and the one received subsequently as ϵ_t and the gained power as ξ_t, with mathematical representations

$$\begin{cases} \epsilon_t = P_t^{\mathrm{BS}} - \eta_t^{\mathrm{up}} \alpha P_t^{\mathrm{UD}} = (1 - \alpha \eta_t^{\mathrm{up}} \eta_t^{\mathrm{down}}) P_t^{\mathrm{BS}} \\ \xi_t = P_{t+1}^{\mathrm{BS}} - \alpha \eta_t^{\mathrm{up}} \eta_t^{\mathrm{down}} P_t^{\mathrm{BS}} \end{cases}. \tag{28}$$

Intuitively, when the resonance is established, ϵ and ξ should converge, which means that the power lost on the transmission and harvested by UD is exactly compensated by the power amplifier. When the resonance has yet to be achieved, the power gain should always be greater than the loss, pushing the system to transmit with greater power in an attempt to reach a stable state. The process can be formally put as

$$\begin{cases} \xi_1 > \epsilon_1 \\ \xi_{t\to\infty} = \epsilon_{t\to\infty} \end{cases}. \tag{29}$$

2) Phase Synchronization: Recovering the phase of the received signal is crucial in the proposed system. Apart from performing coherent demodulation, the antenna array needs to acquire the phase information to ensure retro-directive transmitting. Thus, the PLL is introduced. PLLs are designed to synchronize with the phase of the input signal. Incorporated with a voltage-controlled oscillator (VCO), the output of PLL is a sinusoidal wave with the same frequency and phase [30]. However, there are inevitable delays and errors attributed to various factors. First, with the principle of VCO, the output signal is expected to asymptotically approximate the input, but it is not possible to be the same [31]. Suppose the PLLs employed in the system are identical, this part of the error can be considered constant offset and delay across different units. Additionally, circuitry components are subject to multiple noises, this part of the error varies across different processing units since it typically has a stochastic behavior. Hereinafter, we examine the constant phase delay and stochastic phase noise separately to demonstrate the system's feasibility and robustness against phase noises.

Taking summation on m of the complex amplitude given in (15), we can obtain the total field arriving at n-th Rx unit, with a phase term

$$\varphi_n = k\mathbf{r}_n + \omega t - \varphi_0, \tag{30}$$

where the φ_0 is the initial phase term of the superimposed field. With a constant phase delay ψ, the output from PLL is with a phase term

$$\hat{\varphi}_n = k\mathbf{r}_n + \omega t - \varphi_0 + \psi. \tag{31}$$

The output signal subsequently undergoes mixing and filtering to have its phase conjugated and frequency converted, with the resultant phase

$$\hat{\varphi}_n^* = -k\mathbf{r}_n - \omega' t + \varphi_0 - \psi, \tag{32}$$

where ω' is the converted angular frequency.

As mentioned before, the PLLs employed among every processing unit are identical, leading to an identical delay across different units. Thus, the electric field eventually emitted from the Tx array can be obtained as

$$\begin{aligned} \mathbf{E}_{\text{emit}} &= \sum_n A_n \exp(-j(k\mathbf{r}_n + \omega' t - \varphi_0 + \psi)) \\ &= \sum_n A_n \exp\left(-j(k\mathbf{r}_n + \omega' t - \varphi_0)\right) \exp\left(-j\psi\right). \\ &= \exp\left(-j\psi\right) \sum_n A_n \exp\left(-j(k\mathbf{r}_n + \omega' t - \varphi_0)\right) \end{aligned} \tag{33}$$

Given that the phase delay remains constant across time and different units, the delay term can be moved outside the summation. The retro-directivity, fundamentally dependent on the relative phase differences among units, thus persists notwithstanding the presence of the phase delay.

Despite the constant phase delays, components like PLLs are subject to phase noises, which cannot be treated as constant. Stochastic phase noises among different units hamper the relative phase difference, thus hamper the retro-directivity.

In numerical simulations, the phase noises can be studied by subjecting each processing unit to an independently and identically distributed (i.i.d.) Gaussian noise with zero mean and variance equals that of the phase noise. Typically, the phase noise as a parameter of PLL is given in power spectral density (PSD) form and measured in $\mathrm{dBc/Hz}$. Suppose the

PLL is with phase noise power PSD $P(f)$, the variance of the phase noise can be calculated as

$$\sigma_\phi^2 = 2\int_{f_\mathrm{L}}^{f_\mathrm{U}} \mathcal{L}\left(P(f)\right) \mathrm{d}f, \tag{34}$$

where $\mathcal{L}(x) = 10^{\frac{x}{10}}$ is the decibel-to-power conversion function, f_L and f_U denote the lower and upper bound for the offset frequency. The integral is multiplied by two as the PSD function is single-sided.

Intuitively, the phase noise leads to power leakage and signal dispersion, hindering the ability of emitted signals to interfere constructively and form the desired beam perfectly. However, through the iterative establishment of resonance, minor phase noise can be gradually rectified with each iteration. Consequently, despite the presence of phase noise, the beam retains its retro-directive capability, with only negligible power leakage.

C. Communication Channel

Distinguished from the power harvesting that begins in the first iteration, communication is configured to initiate after the stable resonance is achieved. Both the BS and UD are equipped with modulators, with which the information is first modulated onto the LO and subsequently applied to the signal to be transmitted. With the stable resonance, the signal is expected to travel along the shortest and power-focused path between BS and UD, thereby substantially mitigating the multipath effect.

The communication of the resonant beam system can be regarded as a linear time-invariant system [32]. For the downlink, suppose the source signal to be transmitted is $s_\mathrm{in}(t)$, the output signal received at UD can be expressed as

$$s_\mathrm{out}(t) = \gamma P_\mathrm{R} s_\mathrm{in}(t) * h(t) + n(t), \tag{35}$$

where γ is a pre-defined coefficient of which part of the received power is used for communication, $h(t)$ is the channel impulse response, and $n(t)$ is the additive white Gaussian noise, which can be estimated with the noise figures of the employed components.

The signal-to-noise ratio (SNR) of the system is then obtained as

$$SNR = \frac{\gamma P_\mathrm{R}}{kTBF}, \tag{36}$$

where k is Boltzmann's constant, T is the operating temperature measured in Kelvin, B is the system bandwidth, and F is the cascaded noise figure of the receiver, which can be calculated with the Friis cascading equation [33]:

$$F = F_1 + \frac{F_2 - 1}{G_1} + \frac{F_3 - 1}{G_1 G_2} + \cdots + \frac{F_n - 1}{G_1 G_2 \cdots G_{n-1}}, \tag{37}$$

where G denotes the gain for respective subscripts.

In our system, since the returned power from UD to BS is much less than the downlink power, the split ratio for communication use is set to $10 \times \gamma$ for the uplink to maintain an adequate power level for the information transfer. The rest of the configuration and analysis for uplink share the same as those for downlink.

The spectral efficiency of the proposed system can be evaluated using a model [34] prevalent in assessing LTE channels [35], [36]:

$$\tilde{C} = \min\left\{\log_2\left(1 + 10^{0.1(\mathrm{SNR}-\Delta)}\right), C_\mathrm{max}\right\}, \tag{38}$$

with SNR and channel loss factor Δ given in dB. $\tilde{C}$ is the approximate spectral efficiency in bps/Hz and is capped by the maximum C_max, which is determined by the coding. The model has provided a theoretical approach to estimate the channel performance and has been proven to be plausible in the context of mmWave [37], [38].

IV. Performance Evaluation

In this section, various aspects of the system have been assessed to comprehensively demonstrate the performance of the system. Comparative experiments suggested enhancements in both power transfer efficiency and communication performance.

A. Parameters

An exemplary set of parameters are presented in Table I. Parameters of the PLL and power amplifier are taken from [39] [40], respectively. Notably, the parameters of the system can be modified given appropriate and corresponding modifications on the components.

TABLE I
System Parameters

Device	Parameter	Symbol	Value
Base Station	Tx frequency	f_1	28GHz
	Tx antenna spacing	d_1	5.4mm
	Rx frequency	f_2	32GHz
	Rx antenna spacing	d_2	4.7mm
	Number of antenna pairs	$N \times N$	50×50
	Amplifier gain	G_A	15 dB [40]
	Variance of phase noise	σ_ϕ^2	310.17 mrad/s [39]
	Cascaded noise figure	F_B	5 dB [37]
User Device	Tx frequency	f_2	32GHz
	Tx antenna spacing	d_2	4.7mm
	Rx frequency	f_1	28GHz
	Rx antenna spacing	d_1	5.4mm
	Number of antenna pairs	$N \times N$	50×50
	Variance of phase noise	σ_ϕ^2	310.17 mrad/s [39]
	Cascaded noise figure	F_M	7 dB [37]
Gobal Parameters	Modulation scheme	-	QPSK
	System bandwidth	B	500MHz
	Throughput rate	R_b	1Gbps

The micro-strip antenna is adopted as the array units, of which its gain pattern is presented in [41] and visually illustrated in Fig. 7. We suppose that both transmitting and receiving modes share the same gain pattern.

B. Initialization of Resonance

The initialization procedure begins with the UD broadcasting an omnidirectional signal. Upon capturing the signal, BS performs phase conjugation and power amplification before

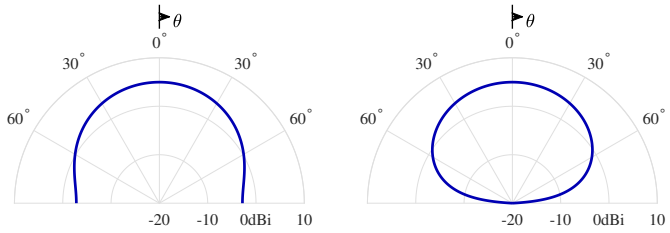

(a) Gain at $\phi = 0°/360°$ (b) Gain at $\phi = 90°/270°$

Fig. 7. Antenna gain $G(\theta, \phi)$.

transmitting back. UD harvests the received power and returns the rest of the power with a fixed ratio α to complete one iteration. The convergence is determined with the power criteria developed in Sec. III. In numerical simulations, if the difference in received power between two consecutive iterations is less than a specific threshold, set to 1% in the following simulations, the system can be considered converged, and the resonance is initialized.

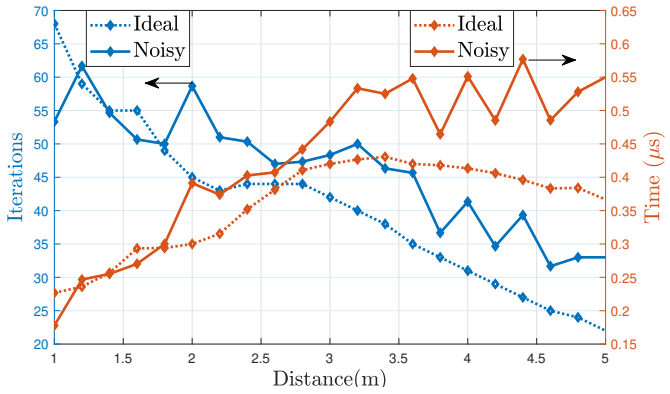

Fig. 8. Iterations and time required as distance increases.

The required time to initialize the resonance is crucial for evaluating the performance of the proposed system. In particular, some application scenario may require no perceptible delay. Intuitively, the time to establish the resonance is the total distance that the EM wave needs to travel divided by the speed of it. Namely,

$$t = \frac{2Ln_{\text{itr}}}{c}, \tag{39}$$

where L is the distance between the Tx and Rx, n_{itr} is the number of iterations required to initialize, and c is the speed of light. The multiplication by 2 accounts for the fact that an iteration consists of two single-trips. Thus, the delay time before the system can provide service can be determined.

Fig. 8 illustrates the iterations and time required before the system converges, where dotted lines represent ideal scenarios and solid lines denote cases affected by phase noise. To smooth out randomness, the data of noisy cases are the mean value of three independently conducted experiments. It is evident that phase noise prolongs the initialization of resonance iterations and introduces performance fluctuations. As the distance between BS and UD increases, fewer iterations are required as the wave superimposition gets more stable with a longer distance. It is also intuitive to understand that with a longer distance, as the single round-trip takes more time, the total time required also increases.

The initialization of the resonance is also visually represented in Fig. 9, with transmission distance set to $d = 3$ m. The power distribution received by UD is illustrated with the rectangle indicating the effective Rx area. The power distribution has been normalized to better present the trend across different iterations. Initially, there are obvious sidelobes outside of the receiving array of UD, leading to power leakage. With successive iterations, a focusing trend is observed as the sidelobes diminish, culminating in a dominant main lobe with negligible side lobes after the resonance is initialized.

The convergence process is analyzed in terms of transmission efficiency and power, as illustrated in Fig. 10, of which the left Y-axis is for transmission efficiency and the right one is for transmitted power. Dotted lines are used for the ideal cases without phase noises, and solid lines with triangle markers are for the real cases. Despite a jittering pattern, the performance under the impact of phase noise agrees with the ideal cases. Both the downlink and uplink exhibit an improvement in transmission efficiency as the iterations progress, reaching a maximum with resonance establishment denoted by the vertical dotted line. The transmission efficiency for both downlink and uplink surpasses 90% with stable resonance, demonstrating the power concentrating feature. The downlink transmitted power, i.e., power from BS to UD, peaks after the resonance is established, at approximately 40 dBm, with the returning power around 13 dBm. This means that more than 20 dBm of power can be harvested by the UD for charging output and information retrieval.

C. Power Transmission and Circulation

We compute the transmission efficiency with (20) for both the proposed system and conventional retro-directive beamforming system, with the results presented in Fig. 11. Intuitively, the transmission efficiency is negatively related to the distance, and phase noise subjects the performance to jitter. It can be observed that, even with the presence of noises, the RBS outperforms the conventional beamforming in terms of transmission efficiency, exhibiting its power concentration feature.

The spatial distribution of power under the case $d = 3$m is depicted in Fig. 12. It should be noted that the power distribution has been logarithmically normalized to better present the detail. It can be observed clearly that RBS features a stronger power beam emitted from BS with sidelobes significantly suppressed. Power returning from UD to BS also forms a focused beam in the case of RBS, making it potent to carry uplink information and thus realize duplex SWIPT.

Compared with traditional retro-directive beamforming only the BS is equipped with RDA, our proposed system enjoys higher power transmission efficiency with its power beam highly focused onto the UD. The system is capable of realizing uplink information transmission since the power returned from UD is also focused, providing adequate power for information transmission.

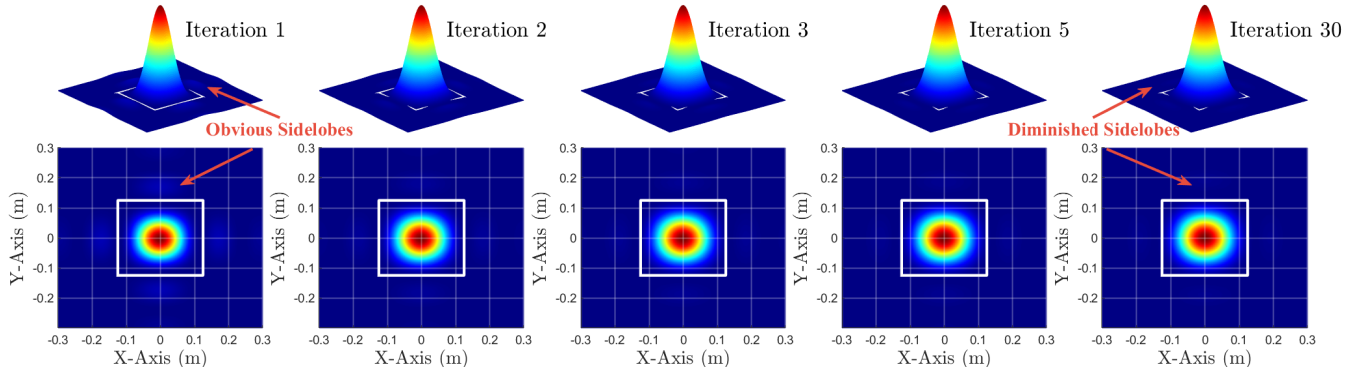

Fig. 9. Received power distribution on UD across successive iterations. Array size indicated by rectangles

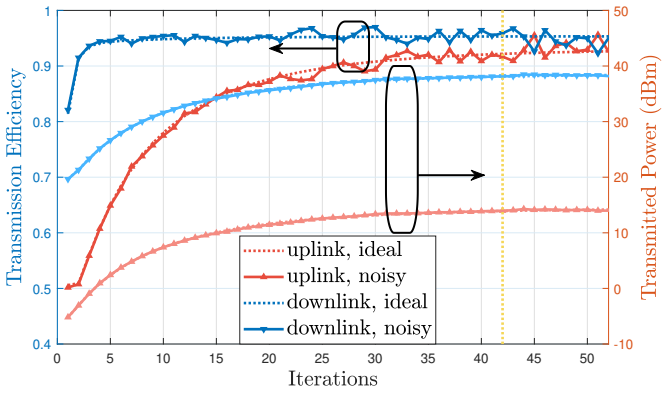

Fig. 10. Transmission efficiency and power across successive iterations.

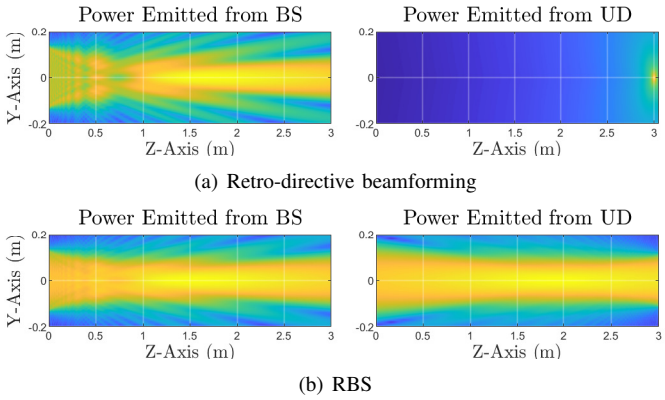

Fig. 12. Spatial distribution of power.

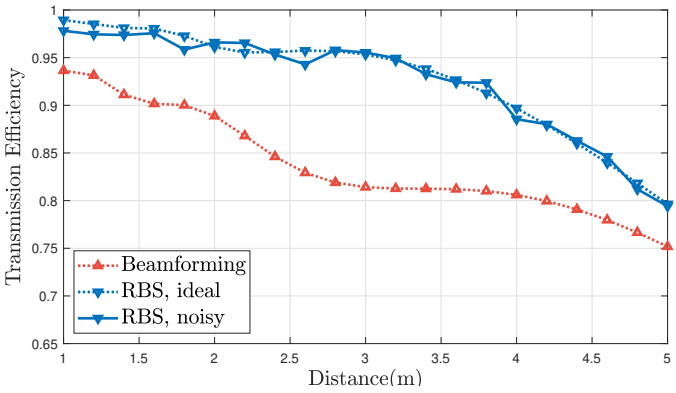

Fig. 11. Transmission efficiency with different distances.

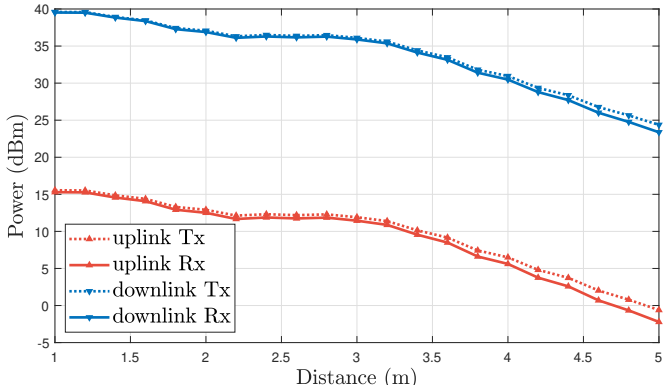

Fig. 13. Power circulation with different distances.

The circulating power after the resonance is established is illustrated in Fig. 13 and measured in dBm. For visual brevity, only the case with phase noise is plotted here. Downlink Rx represents the actual power received by UD, of which 99% is harvested for charging and 0.6% for information retrieval. Uplink Tx represents the power returned from UD to maintain the stable resonance as well as carry the uplink information. The power received by BS for uplink information transmission is indicated by the uplink Rx. Though the circulating power decreases with distance, it can still provide more than 20 dBm for charging the UD even with a distance of 5 m.

D. Communication Performance

As explicated before, the communication link is only established after a stable resonance is achieved, aiming to provide better communication performance. Therefore, the proposed system exhibits high SNR compared to similar works in the realm of mmWave.

On the UD side, the majority of the received power is to be harvested for DC output, leaving only $\gamma = 0.6\%$ of the power for information transmission. As for the BS, 6% of the received power is taken to ensure that BS can have enough power for uplink information reception.

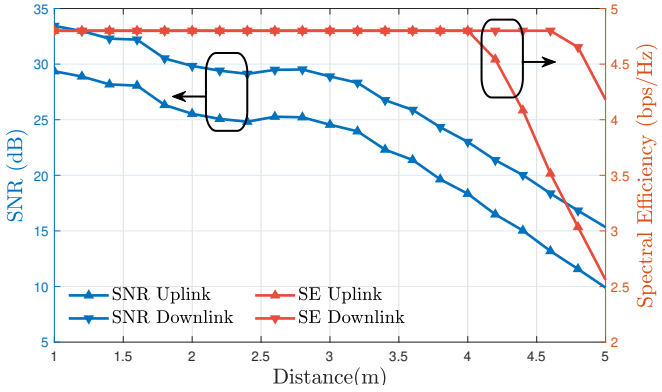

Fig. 14. SNR and spectral efficiency.

SNR and spectral efficiency (SE) performance are shown in Fig. 14. Benefiting from the resonance, both downlink and uplink enjoy SNR above 0 dB with a 5 m transmission distance. Spectral efficiency is calculated based on the parameters derived in [37], where loss factor $\Delta = 3$ dB and maximum SE $C_{\max} = 4.8$ bps/Hz. With only a very small portion of power returned from UD as the uplink, it is natural that the uplink underperforms the downlink with respect to both SNR and SE. However, within the indoor application environment, the system is still capable of providing a stable duplex communication link with a high throughput rate.

V. Discussion

In this section, several topics regarding the proposed system is explored and discussed to provide a preliminary perspective for future works.

A. Robustness against Phase Noise

The principle of the resonant beam system requires the retro-directive antenna array to retro-reflect the received signal. This poses a high demand for the accuracy of the phase recovery. As indicated in the analysis, PLLs are subject to inherent phase noises. The intensity of the phase noise has a crucial impact on the system's ability to converge. Fig. 15 depicts the power distribution from both BS and UD with different phase noise variance σ_ϕ^2 in $\mathrm{mrad/s}$.

It can be seen from Fig. 15 that phase noise hinders the system convergence by causing fluctuations close to the antenna array, whereas the overall retro-directivity is not severely affected. As the phase noise gets stronger, the fluctuations increase as well. The PLL we adopted is with a phase noise variance $\sigma_\phi^2 \approx 310.17$ [39], which does not impose severe damage to the resonance initialization process. If the noise continues to increase when $\sigma_\phi^2 = 500$, the system is still capable of reaching stable status despite a reduced power focusing ability. This will lead to less power available for charging and lower channel SNR. Under the condition $\sigma_\phi^2 = 800$, the fluctuations are over dominant so that there is almost no power for the system function.

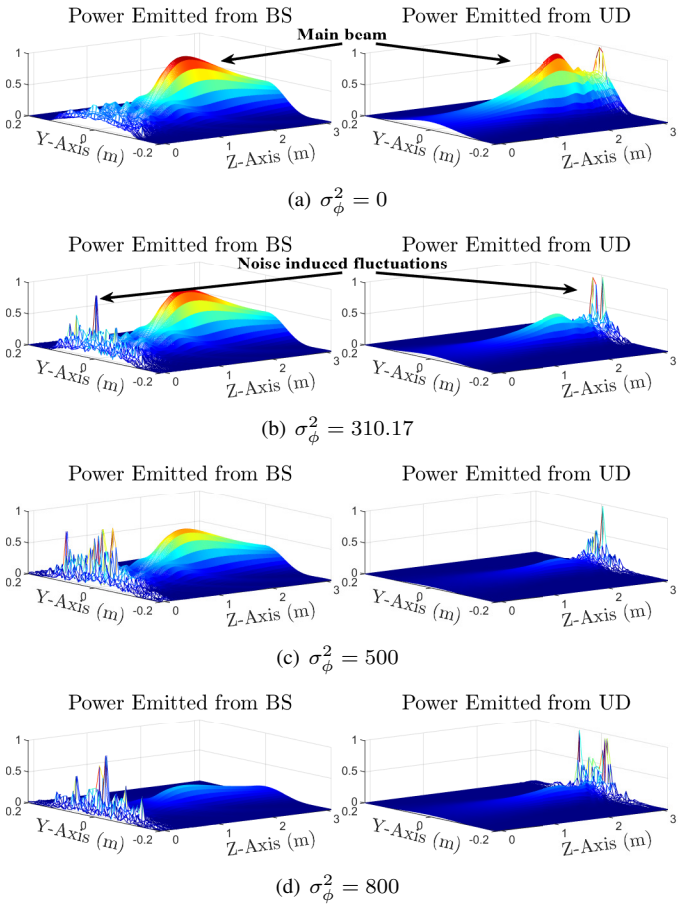

(a) $\sigma_\phi^2 = 0$

(b) $\sigma_\phi^2 = 310.17$

(c) $\sigma_\phi^2 = 500$

(d) $\sigma_\phi^2 = 800$

Fig. 15. Power distribution under different conditions.

B. Power Splitting Ratio

The power splitting ratio for signal processing, power harvest, and information retrieving is of great significance. The power received by the UD is splitted into three part: i) energy harvest, ii) information retrieval, and iii) return to BS. To avoid ambiguity, we adopt the following notations for further discussion.

$$\begin{cases} P_{\text{return}} = \alpha P_{\text{R}} \\ P_{\text{charge}} = \beta P_{\text{R}} \\ P_{\text{comm}} = \gamma P_{\text{R}} \\ \alpha + \beta + \gamma = 1 \end{cases}, \tag{40}$$

where P_{R} is the total power received by UD, P_{return}, P_{charge}, and P_{comm} denote the power for return, energy harvest, and downlink communication respectively.

The optimal solution for UD is to maximize the power available for charging as well as return adequate power for the uplink information carrier. In Fig. 13, the downlink power is above 20 dBm even with a transmission distance at 5 m. With $\gamma = 0.6\%$, we have the downlink communication power $P_{\text{comm}} \approx 2$ dBm, which is well adequate for wireless communication.

However, for the uplink communication, there is a trade-off between the communication and power harvest. The BS is designed to divide a part of the returned power to retrieve the

uplink information, in our configuration, the ratio is 10γ. The power available for uplink communication can be put as:

$$P'_{\text{comm}} \leq 10\alpha\gamma P_{\text{R}}. \tag{41}$$

The inequality accounts for the over-the-air transmission loss on the uplink. Intuitively, if we increase the value of α, we could have more power available for uplink communication, but less power for the UD to harvest. However, the numerical simulation has suggested a counter-intuitive conclusion, i.e., increasing α will lead to more power available for charging the UD. This is due to the resonance principle, as the returned power increases, the system is stimulated to operate with higher power. The results with different α values are outlined in Table II.

TABLE II
POWERS WITH DIFFERENT α

α	**Charging Power** (dBm)	**Downlink Comm. Power** (dBm)	**Uplink Comm. Power** (dBm)
0.2%	18.982	−3.202	−20.608
0.3%	26.204	4.025	−11.781
0.4%	35.224	13.049	−1.445

Moreover, the return ratio α also has impact on the efficiency of the system. Excessively high α may force the power amplifiers to a saturation state, thus reducing the overal efficiency and prolong the initialization of stable resonance. The maximum allowed value for α may vary depending on the configuration of antenna and other components. With our current parameters in Table I., the α is limited below 0.5%. If the returned power is excessively high, the system will be pushed to a saturated state where every power amplifier works in saturation state, resulting in decline of overall efficiency and negative impact on the retro-directivity.

C. Radiation Hazard and Safety Concerns

In practical application, the radiation hazard of wireless systems is of great concerns. In this paper, the proposed system employs mmWave as the spatial carrier of power and information. The main safety concern over mmWave radiation is the heat absorbed by eyes and skins since the radiation is non-ionizing [42], [43]. To assess the radiation of signals with frequency range from 10 GHz to 300 GHz, the power density is adopted as the main measurement, with W/m^2 as the unit [43]. A guideline from the International Commission on Non-Ionizing Radiation Protection (ICNIRP) suggested a power density of 200 W/m^2 averaged over 6 minutes and a square 4 cm^2 surface area as the local exposure threshold for EM fields in this frequency range [44].

Being different from the traditional wireless power transmitter that continuously emits power, the BS in our proposed system requires the resonant feedback from UD to amplify and emit the power beam, thus maintaining the resonance. In the case where human body obstructs the resonant beam, the power lost over the air (OTA) would increase drastically, resulting in the resonance being cut off. Referring to (28), ξ is the power gained from amplification process, of which the maximum possible value is determined by the power amplifier.

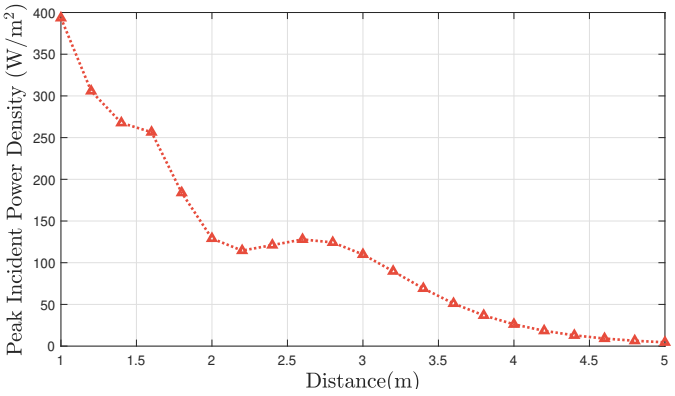

Fig. 16. Instantaneous peak power density incident on the invading object.

During the human invasion, the transmission efficiencies of both downlink and uplink drop significantly, leading to a large ϵ. Once the power lost exceed the maximum allowed power gain, i.e., $\epsilon > \xi$, the resonance is destroyed automatically. The resonance cannot be re-initiate before the obstruction is cleared. Therefore, the only radiation cast on the invading object is the portion of power that is already OTA, the radiation is instantaneous instead of continuous.

A preliminary simulation is conducted supposing the invading object obstructs the beam completely. The instantaneous peak power density incident on the invading object is depicted in Fig. 16. The x-axis of Fig. 16 is the distance between BS and UD of the system. The obstacle is set to have a constant distance of 0.5 m from the BS. In the small distance setup, the peak power density seems to exceed the maximum allowed by the guidline. However, since the resonance is immediately cut off after invasion, the object will not be radiated continuously. If the power density is averaged over a time span of 6 minutes according to the ICNIRP guideline, the exposure level is reduced to a negligible order of 10^{-6} W/m^2 since the power radiation is relaxed within 1 μs.

Obstacle invasion to the resonance has also been studied in the realm of the optical RBS. The inherent safety feature of the RBS is comprehensively examined in [45], where analytical models are established to investigate the electromagnetic behavior of the system during the invasion.

VI. CONCLUSION

A mmWave-based resonant beam system is proposed in this manuscript to provide simultaneous wireless power and information transfer. By employing retro-directive antenna arrays on both the base station and the user device, the signal can be reflected back and forth between the cavity formed by the transceiver pair, thus enabling automatic beam alignment without the extra need for beam control mechanisms. With the iterative initialization process, the system is capable of focusing the power onto a narrow beam similar to a laser, thus enjoying a high power transfer efficiency and high SNR for communication.

Frequency division duplex communication is enabled with a special design to allow the system to operate with different

frequencies for downlink and uplink without losing the retro-directive feature.

The performance of the proposed system is demonstrated with simulations conducted with MATLAB. We take an iterative approach to verify that the system can converge within less than 1μs. The system is proved to be robust against the phase noises imposed by the components. Simulation results also suggested that the proposed system is capable of providing approximately 1W of charging power with 4.8bps/Hz of channel spectral efficiency.

Future development of the system can be focused on the scale of the antenna array and dedicated component design. In this manuscript, we take the off-the-shelf RF components which are not initially designed for such usage. Smaller antenna scales and special designs for the RF components hold the potential to enhance the system's performance and practicality. Furthermore, apart from topics discussed in the previous section, future works may also consider incorporating circuit simulations and realistic experiments to further evaluate the performance of the proposed system under realistic circumstances.

REFERENCES

[1] Z. Wei, H. Qu, Y. Wang, X. Yuan, H. Wu, Y. Du, K. Han, N. Zhang, and Z. Feng, "Integrated sensing and communication signals toward 5G-A and 6G: A survey," *IEEE Internet of Things Journal*, vol. 10, no. 13, pp. 11 068–11 092, 2023.

[2] A. Costanzo, D. Masotti, G. Paolini, and D. Schreurs, "Evolution of SWIPT for the IoT world: Near- and far-field solutions for simultaneous wireless information and power transfer," *IEEE Microwave Magazine*, vol. 22, no. 12, pp. 48–59, 2021.

[3] K. W. Choi, S. I. Hwang, A. A. Aziz, H. H. Jang, J. S. Kim, D. S. Kang, and D. I. Kim, "Simultaneous wireless information and power transfer (SWIPT) for Internet of Things: Novel receiver design and experimental validation," *IEEE Internet of Things Journal*, vol. 7, no. 4, pp. 2996–3012, 2020.

[4] T. D. P. Perera, D. N. K. Jayakody, S. K. Sharma, S. Chatzinotas, and J. Li, "Simultaneous wireless information and power transfer (SWIPT): Recent advances and future challenges," *IEEE Communications Surveys & Tutorials*, vol. 20, no. 1, pp. 264–302, 2017.

[5] D. Xu and H. Zhu, "Secure transmission for SWIPT IoT systems with full-duplex IoT devices," *IEEE Internet of Things Journal*, vol. 6, no. 6, pp. 10 915–10 933, 2019.

[6] B. Clerckx, A. Costanzo, A. Georgiadis, and N. Borges Carvalho, "Toward 1g mobile power networks: Rf, signal, and system designs to make smart objects autonomous," *IEEE Microwave Magazine*, vol. 19, no. 6, pp. 69–82, 2018.

[7] M. Liu, H. Deng, Q. Liu, J. Zhou, M. Xiong, L. Yang, and G. B. Giannakis, "Simultaneous mobile information and power transfer by resonant beam," *IEEE Transactions on Signal Processing*, vol. 69, pp. 2766–2778, 2021.

[8] Y. Bai, Q. Liu, L. Yang, G. B. Giannakis, W. Fang, and M. Xiong, "Resonant beam SWIPT with telescope and second harmonic," *IEEE Transactions on Wireless Communications*, 2022.

[9] S. Xia, Q. Liu, M. Liu, W. Fang, M. Xiong, Y. Bai, and X. Li, "Auto-protection for resonant beam SWIPT in portable applications," *IEEE Internet of Things Journal*, 2023.

[10] T. Matsumuro, Y. Ishikawa, and N. Shinohara, "Basic study of both-sides retrodirective system for minimizing the leak energy in microwave power transmission," *IEICE Transactions on Electronics*, vol. 102, no. 10, pp. 659–665, 2019.

[11] M. Xiong, Q. Liu, G. Wang, G. B. Giannakis, and C. Huang, "Resonant beam communications: Principles and designs," *IEEE Communications Magazine*, vol. 57, no. 10, pp. 34–39, 2019.

[12] M. Xiong, Q. Liu, G. Wang, G. B. Giannakis, S. Zhang, J. Zhu, and C. Huang, "Resonant beam communications with echo interference elimination," *IEEE Internet of Things Journal*, vol. 8, no. 4, pp. 2875–2885, 2020.

[13] W. Hong, Z. H. Jiang, C. Yu, D. Hou, H. Wang, C. Guo, Y. Hu, L. Kuai, Y. Yu, Z. Jiang *et al.*, "The role of millimeter-wave technologies in 5G/6G wireless communications," *IEEE Journal of Microwaves*, vol. 1, no. 1, pp. 101–122, 2021.

[14] L. Wang, M. Elkashlan, R. W. Heath, M. Di Renzo, and K.-K. Wong, "Millimeter wave power transfer and information transmission," in *2015 IEEE Global Communications Conference (GLOBECOM)*, 2015, pp. 1–6.

[15] C. Liu, M. Li, S. V. Hanly, I. B. Collings, and P. Whiting, "Millimeter wave beam alignment: Large deviations analysis and design insights," *IEEE journal on selected areas in communications*, vol. 35, no. 7, pp. 1619–1631, 2017.

[16] L.-T. Tu and M. Di Renzo, "Analysis of millimeter wave cellular networks with simultaneous wireless information and power transfer," in *2017 International Conference on Recent Advances in Signal Processing, Telecommunications Computing (SigTelCom)*, 2017, pp. 39–43.

[17] X. Wang, S. Sha, J. He, L. Guo, and M. Lu, "Wireless power delivery to low-power mobile devices based on retro-reflective beamforming," *IEEE Antennas and Wireless Propagation Letters*, vol. 13, pp. 919–922, 2014.

[18] H. Koo, J. Bae, W. Choi, H. Oh, H. Lim, J. Lee, C. Song, K. Lee, K. Hwang, and Y. Yang, "Retroreflective transceiver array using a novel calibration method based on optimum phase searching," *IEEE Transactions on Industrial Electronics*, vol. 68, no. 3, pp. 2510–2520, 2021.

[19] Y. Jiang, B. Liu, W. Li, B. Zhu, J. Cao, and X. Wang, "Retro-reflective beamforming to multiple targets based on time-reversal for microwave power transmission," in *2022 IEEE MTT-S International Wireless Symposium (IWS)*, vol. 1. IEEE, 2022, pp. 1–3.

[20] R. Miyamoto and T. Itoh, "Retrodirective arrays for wireless communications," *IEEE Microwave Magazine*, vol. 3, no. 1, pp. 71–79, 2002.

[21] R. Miyamoto, Y. Qian, and T. Itoh, "A reconfigurable active retrodirective/direct conversion receiver array for wireless sensor systems," in *2001 IEEE MTT-S International Microwave Sympsoium Digest (Cat. No.01CH37157)*, vol. 2, 2001, pp. 1119–1122 vol.2.

[22] C. W. Pobanz and T. Itoh, "A conformal retrodirective array for radar applications using a heterodyne phased scattering element," in *Proceedings of 1995 IEEE MTT-S International Microwave Symposium*. IEEE, 1995, pp. 905–908.

[23] S.-C. Yen and T.-H. Chu, "A retro-directive antenna array with phase conjugation circuit using subharmonically injection-locked self-oscillating mixers," *IEEE Transactions on Antennas and Propagation*, vol. 52, no. 1, pp. 154–164, 2004.

[24] Y. Kang, X. Q. Lin, Y. Li, and B. Wang, "Dual-frequency retrodirective antenna array with wide dynamic range for wireless power transfer," *IEEE Antennas and Wireless Propagation Letters*, vol. 22, no. 2, pp. 427–431, 2022.

[25] D. Dardari, M. Lotti, N. Decarli, and G. Pasolini, "Establishing multi-user mimo communications automatically using retrodirective arrays," *IEEE Open Journal of the Communications Society*, vol. 4, pp. 1396–1416, 2023.

[26] M. Liu, G. Wang, G. B. Giannakis, M. Xiong, Q. Liu, and H. Deng, "Wireless power transmitter deployment for balancing fairness and charging service quality," *IEEE Internet of Things Journal*, vol. 7, no. 3, pp. 2223–2234, 2020.

[27] W. Fang, G. Wang, G. B. Giannakis, Q. Liu, X. Wang, and H. Deng, "Channel-dependent scheduling in wireless energy transfer for mobile devices," *IEEE Transactions on Vehicular Technology*, vol. 69, no. 3, pp. 3330–3340, 2020.

[28] F. T. Ulaby and U. Ravaioli, *Fundamentals of applied electromagnetics*. Pearson Upper Saddle River, NJ, 2015, vol. 7.

[29] C. M. Song, S. Trinh-Van, S.-H. Yi, J. Bae, Y. Yang, K.-Y. Lee, and K. C. Hwang, "Analysis of received power in RF wireless power transfer system with array antennas," *IEEE Access*, vol. 9, pp. 76 315–76 324, 2021.

[30] T. Edwards, *Technologies for RF Systems*. USA: Artech House, Inc., 2018.

[31] F. Dowla, *Handbook of RF and wireless technologies*. Elsevier, 2003.

[32] M. Xiong, M. Liu, Q. Jiang, J. Zhou, Q. Liu, and H. Deng, "Retro-reflective beam communications with spatially separated laser resonator," *IEEE Transactions on Wireless Communications*, vol. 20, no. 8, pp. 4917–4928, 2021.

[33] F. Ellinger, *Radio frequency integrated circuits and technologies*. Springer Science & Business Media, 2008.

[34] P. Mogensen, W. Na, I. Z. Kovacs, F. Frederiksen, A. Pokhariyal, K. I. Pedersen, T. Kolding, K. Hugl, and M. Kuusela, "LTE capacity com-

pared to the Shannon bound," in *2007 IEEE 65th Vehicular Technology Conference - VTC2007-Spring*, 2007, pp. 1234–1238.

[35] E. J. Oughton, Z. Frias, S. van der Gaast, and R. van der Berg, "Assessing the capacity, coverage and cost of 5G infrastructure strategies: Analysis of the netherlands," *Telematics and Informatics*, vol. 37, pp. 50–69, 2019.

[36] S. H. A. Shah, S. Aditya, and S. Rangan, "Power-efficient beam tracking during connected mode drx in mmwave and sub-thz systems," *IEEE Journal on Selected Areas in Communications*, vol. 39, no. 6, pp. 1711–1724, 2021.

[37] M. R. Akdeniz, Y. Liu, M. K. Samimi, S. Sun, S. Rangan, T. S. Rappaport, and E. Erkip, "Millimeter wave channel modeling and cellular capacity evaluation," *IEEE Journal on Selected Areas in Communications*, vol. 32, no. 6, pp. 1164–1179, 2014.

[38] S. Dutta, C. N. Barati, D. Ramirez, A. Dhananjay, J. F. Buckwalter, and S. Rangan, "A case for digital beamforming at mmwave," *IEEE Transactions on Wireless Communications*, vol. 19, no. 2, pp. 756–770, 2019.

[39] J.-Y. Lee, S.-H. Lee, H. Kim, and H.-K. Yu, "A 28.5–32-GHz fast settling multichannel PLL synthesizer for 60-GHz WPAN radio," *IEEE Transactions on Microwave Theory and Techniques*, vol. 56, no. 5, pp. 1234–1246, 2008.

[40] "HMC1132PM5E datasheet and product info — analog devices." [Online]. Available: https://www.analog.com/media/en/technical-documentation/data-sheets/HMC1132PM5E.pdf

[41] C. A. Balanis, *Antenna theory: analysis and design*. John wiley & sons, 2016.

[42] T. Wu, T. S. Rappaport, and C. M. Collins, "The human body and millimeter-wave wireless communication systems: Interactions and implications," in *2015 IEEE International Conference on Communications (ICC)*, 2015, pp. 2423–2429.

[43] R. Dilli, "Implications of mmwave radiation on human health: State of the art threshold levels," *IEEE Access*, vol. 9, pp. 13 009–13 021, 2021.

[44] I. C. on Non-Ionizing Radiation Protection *et al.*, "Guidelines for limiting exposure to electromagnetic fields (100 kHz to 300 GHz)," *Health physics*, vol. 118, no. 5, pp. 483–524, 2020.

[45] W. Fang, H. Deng, Q. Liu, M. Liu, Q. Jiang, L. Yang, and G. B. Giannakis, "Safety analysis of long-range and high-power wireless power transfer using resonant beam," *IEEE Transactions on Signal Processing*, vol. 69, pp. 2833–2843, 2021.